

J6J.3 THE STRUCTURE AND EVOLUTION OF THE DRYLINE AND SURROUNDING BOUNDARY LAYER ON 22 MAY 2002 DURING IHOP

Michael S. Buban¹, Conrad L. Ziegler², Erik N. Rasmussen¹, and Yvette P. Richardson³

¹Cooperative Institute for Mesoscale Meteorological Studies (CIMMS), University of Oklahoma, Norman OK

²NOAA/National Severe Storms Laboratory, Norman OK

³Department of Meteorology, Pennsylvania State University, State College PA

1. INTRODUCTION

Surface boundaries such as fronts (e.g. Carbone 1982; Nielsen and Nielley 1990), sea-breezes (e.g. Laird et al 1995; Kingsmill 1995), and thunderstorm outflows (e.g. Wakimoto 1982; Mahoney 1988) play an important role in the initiation of deep convection, and thus have been extensively studied. The dryline has also become a subject of increasing interest due to its frequent association with convection initiation (CI) and subsequent development of severe weather (Rhea 1966; Bluestein and Parker 1993). During the Verification of the Origins of Rotation in Tornadoes Experiment or VORTEX (Rasmussen et al 1994), the structure of the dryline was observed in several cases (Atkins et al 1998; Ziegler and Rasmussen 1998; Weiss and Bluestein 2002). Results from these experiments have improved the conceptual model of dryline morphology, though details of the temporal and spatial variability needed to predict convection initiation processes are lacking. Although we have a fairly good understanding of the mesoscale conditions favor storm development, a lack of high resolution observations in many previous studies has precluded an examination of the very small, kilometer-scale processes which force CI (Johns and Doswell 1992; McNulty 1995).

During the spring and summer of 2002, the International H₂O project (IHOP) was conducted over the southern plains to gain a better understanding of the four-dimensional distribution of water vapor in the atmosphere (Weckwerth et al 2004). One of the main

objectives of this project was to obtain high resolution, small-scale observations of surface-based boundaries and the associated boundary layer (BL) to improve the understanding of cloud-scale CI processes and contribute to development of improved short-range thunderstorm forecasts (Weckwerth and Parsons 2005).

Unlike other boundaries such as fronts or thunderstorm outflows, which generally have strong temporal and spatial dynamical consistency, the dryline is unique in that the dynamics which control its structure and evolution can vary markedly over very short time and space scales. For example, Bluestein et al (1988) and Hane et al (1997) showed observational evidence and Ziegler et al. (1997) showed from a three-dimensional numerical simulation the presence of horizontal along-line variability at the dryline. Others have shown modulation of the dryline structure by temporal and spatial varying frontogenetical processes, such as through vertical transport of westerly momentum, symmetric instability, the inland sea-breeze effect, and waves (Atkins et al. 1998). The dynamics that govern dryline propagation are also unclear. It has been shown that at times the dryline may behave like a density current (Schaefer 1974; Parsons et al. 1991; Ziegler et al. 1995) and at other times may be driven by boundary layer processes (Schaefer 1974; Sun and Wu 1992). The temporal and spatial variability of the dryline and BL structure have significant implications for the convection initiation process.

During the late afternoon and early evening of 22 May 2002, high-resolution data from numerous platforms were collected over the northeast Texas and eastern Oklahoma panhandles in a region where a sharpening dryline had become established. Due to the multitude of observing platforms and the small area of the intensive observing region (IOR), a comprehensive, cloud-scale observational data set of the dryline and its

**Corresponding author address:* Michael S. Buban, National Severe Storms Laboratory, Forecast Research and Development Division, 1313 Halley Circle, Norman, OK 73069.

surrounding environment was obtained for the first time. Analyses of the time-varying 3-D multiple-Doppler wind field are used to assimilate in-situ state data, via a new Lagrangian analysis technique facilitating the derivation of the time-varying 3-D thermodynamic structure of the dryline and its surrounding BL environment. This paper employs the radar, in-situ, and Lagrangian analyses to describe the detailed structure and evolution of the dryline and document potential convection initiation. Radar refractivity and plogometric measurements are used to estimate surface moisture fields and infer secondary circulations along the dryline.

2. DATA COLLECTION AND ANALYSIS

a. IHOP facilities

The IHOP mobile facilities were deployed on the afternoon of 22 May 2002 in the northeast TX and eastern OK panhandles in the anticipation of CI in the vicinity of a developing dryline (Fig. 1a). The dryline began as a weak moisture gradient, which progressively tightened throughout the afternoon. Although there was the potential for deep convection, storms failed to form from the developing cumuli in the intensive observing region (IOR).

Among the platforms participating in the data collection were seven mobile mesonets (MM), which were taking in situ measurements of temperature, relative humidity, pressure, and wind velocity (Straka et al 1996; Ziegler et al 2004). The mobile mesonets performed east-west transects approximately perpendicular to the dryline (Fig. 1b) and collected data at a frequency of 1 Hz. The 5-cm Shared Mobile Atmospheric Research and Teaching (SMART) radar or SR-1 (Biggerstaff et al 1996; Biggerstaff and Guynes 2000) was deployed with the 3-cm, DOW2, DOW3, and X-Pol radars (Wurman et al 1997; Wurman 2001). The mobile ground-based radars were arranged in a diamond pattern (Fig. 1b), with each taking time-synchronized 140° sector scans stepped in elevation and centered on the dryline and completed volumes in 1.5-3 min (Table 1). This configuration was employed to maximize baseline angles and allow for optimal multiple-Doppler wind synthesis. Between 2230 through 0100 UTC (all times are Universal Time) between 3 and 4 mobile radars were obtaining data in the IOR (Table 2). Also participating were a mobile CLASS (Rust et al 1990) and 2 mobile GLASS sounding systems, the Wyoming King Air, the NRL P-3, a Learjet releasing dropsondes, the UAH profiling

system (MIPS), a mobile radiometer (DRI), and a Scanning Raman Lidar (SRI). Also given the proximity of the IOR to the Homestead and S-Pol sites, both Homestead soundings and S-Pol radar data complemented the mobile soundings (Fig 1b).

b. Radar Analysis

In the first step of the radar post-analysis, the data are edited to correct truck orientation relative to due north. This is accomplished in one of two ways. For DOW2, an algorithm is applied to determine truck orientation by comparing the angle of the maximum power returned on a sweep scanning the sun and the known orientation of the sun relative to true north (Arnott et al. 2003). For the other radars a GIS-based technique (Ziegler et al. 2004) is applied to rotate radar sweeps to match up ground targets in the radar data with known locations of the targets. The data are then edited using the NCAR Solo software (Oye et al 1995) to remove ground targets and weak signals and to dealias radial velocities.

A modified version of the NCAR Reorder software (Oye et al 1995) is used to interpolate the edited data to a 50 x 50 x 2.5 km regular Cartesian grid with a grid spacing of 500 m in the horizontal and 250 m in the vertical (101 x 101 x 11 grid points). The interpolation is performed using a Barnes objective analysis scheme. The Barnes weighting function $w = \exp(-r^2/k)$ is used to weight each datum, where r is the distance between the datum and the gridpoint, and k is the smoothing parameter which controls the shape of the response function (Koch et al. 1983). Choosing $k = 0.0486$ yields a response of e^{-1} (37%) at a wavelength $l = 1.1$ km and 5% at $l = 3.1$ km. The Barnes weighting function has been chosen to capture the cloud-scale (~1km) features of the flow while damping the influence of smaller irresolvable scales.

The objectively analyzed velocity data are then combined using the NCAR Cedric software to solve an over-determined set of two linear equations for the triple- or quadruple-Doppler horizontal wind velocities at each grid level (Mohr et al 1986). The vertical velocities are obtained by integrating the mass continuity equation from $w = 0$ at ground level. Time series of triple- or quadruple-Doppler synthesized three-dimensional wind velocities are produced at 3-minute intervals from 2233-0024 (Table 2).

c. Thermodynamic analysis

In-situ data collected from the mobile mesonets, aircraft, and soundings are used to obtain the

thermodynamic characteristics of the dryline and surrounding boundary layer using a Lagrangian objective analysis technique (Ziegler et al 2005). Since in-situ data are collected along one-dimensional transects (i.e. east-west roads, a flight leg) the horizontal resolution is limited by platform spacings. To circumvent this problem, a time-to-space conversion technique has been developed to extract instantaneous 2-D spatial fields from strings of 1-D data in space and time. According to this procedure, data are advected both upstream and downstream along trajectories computed from the time-varying multiple-Doppler synthesized wind fields. The advected MM data are then analyzed to the surface grid using a 2-D Barnes objective analysis scheme. After the initial pass, “pseudo-soundings” and subsequent trajectories are objectively analyzed. The “pseudo-soundings” are produced by mixing percentages of moist- and dry-side “reference” soundings (Fig. 3d) as determined by the local 2-D surface analysis mixing ratio value. For example, if the moist (dry) side surface sounding value is 8 (4) g kg^{-1} and the grid point surface analysis value is 7 g kg^{-1} then the resulting “pseudo-sounding” would consist of a mixture of 75% of the moist side sounding and 25% of the dry side sounding. Trajectories are calculated for these gridpoint sounding values, followed by 3-D objective analyses of all in-situ and gridpoint sounding data to give a 3-D objective analysis. A second 3-D Barnes objective analysis pass is then applied with a convergence parameter $g=0.3$ to recover additional detail from the observations. Finally, a hole-filling procedure is used to eliminate small areas of missing data.

3. ANALYSIS RESULTS

a. Synoptic setting

The large-scale pattern on the afternoon of 22 May exhibited a broad low amplitude ridge over the central United States nestled between a departing short-wave trough over the southeast and approaching trough over the northern intermountain west (e.g. Weiss et al 2005). This pattern featured broad west-southwesterly flow at upper levels and south-southwesterly to southerly flow at low levels over the central and southern plains. In the lee of the Rockies a surface trough and moisture gradient had developed from Nebraska southward through Texas and by afternoon had strengthened to form a pronounced dryline (Fig. 1a). The low levels were warm and moist east of the dryline (Figs. 1a, 2b) and hot and dry to the west of the

dryline (Figs. 1a, 2a, 2c). GOES satellite images show bands of cumulus developing in the vicinity of the dryline by mid afternoon. From late afternoon through early evening the cumulus clouds continued to form but were unable to overcome the convective inhibition to form storms. The dryline began to retrogress back to the west during late afternoon.

b. Radar observations

Multiple-Doppler wind analyses are performed at 3-minute intervals using either 3 or 4 radars from approximately 2230-0030 (Table 2). The dryline is delineated by a nearly north-south oriented band of enhanced reflectivity residing in a zone of confluent flow (Fig 3). East of the dryline the low-level winds are southerly while west of the dryline they are southwesterly. At the top of the boundary layer the winds veer to southwesterly, orienting the dryline nearly along the mean boundary layer flow. Although the primary orientation of the dryline was toward about 20 degrees east of North, several undulations are noted in the reflectivity and velocity analyses, implying that smaller dryline segments may exhibit different orientations. These waves are on the order of 10 to 15 km in wavelength, and appear to ripple along the dryline with the low-level flow. Another surface-based boundary or “secondary dryline” is located about 10 to 15 km west of the primary dryline (see also Fig. 1 for the synoptic setting of the details). This feature exhibits a secondary local maximum in reflectivity and also resides in a region of confluence. It will be shown later that this boundary is also associated with a moisture gradient.

The structure of the boundary layer changes markedly during the period of 2233-0012. The SSW-NNE oriented dryline is initially quasi-stationary, located near X-Pol and Homestead, and is seen as a nearly continuous zone of moderate updrafts with embedded pockets of updrafts greater than 2 m s^{-1} . The boundary layer west of the dryline exhibits a complex structure characterized by both open cellular and longitudinal banded features. These longitudinal horizontal convective rolls become more predominant west of the dryline, while east-west oriented bands of enhanced vertical velocity associated with transverse rolls develop east of the dryline. A band of convergence and stronger upward vertical motion is associated with the secondary dryline. As the dominant convective mode becomes more organized into linear bands, several undulations or waves develop in the regions of dryline/HCR intersections and propagate

from south to north along the dryline. These undulations have wavelengths on the order of 7-8 km and are collocated with stronger vortices. With the loss of surface heating around 0000 UTC the linear bands in the dry air become less organized while the dryline circulation strengthens. This strengthening is associated with a backing of the winds in the moist air and concurrent westward acceleration of the dryline. The smaller scale waves that rippled along the dryline are replaced with larger (~ 15 km wavelength) waves after retrogression begins. As the smaller scale waves, the longer waves also propagate along the dryline at a speed close to the mean boundary layer wind. These waves, termed mesoscale dryline waves or MDLW (Koch 1979), are similar in wavelength to MDLWs reported by McCarthy and Koch (1982). Also, streaks of higher vertical velocities that project eastward over the moist air develop and move along the dryline. These streaks appear to be connected to remnants of HCRs that were lifted at the dryline (Atkins et al 1998).

A strong dryline-normal secondary circulation is evident through the entire analysis period. The strong south-southwesterly flow approaches the dryline from the west. Strong convergence and vertical motion lifts the westerly flow and over the surface dryline location. An opposing flow at low-levels east of the dryline associates with westerly BL flow separation from the surface. Westerly flow subsequently detrains from the updraft. Ziegler and Rasmussen (1998) hypothesized that the air must reach its lifted condensation level (LCL) before detraining from the updraft to form cumulus clouds.

The vertical velocity maximum at the dryline consistent with a maximum in reflectivity as bug scatterers are concentrated and lofted in the updraft. The highest reflectivities are generally contained within the internal boundary layer east of the dryline, with the strongest vertical reflectivity gradient at the transition between the internal and the external boundary layers. Evidence of the lifting of scatterers by the updrafts can also be seen by the correspondence between reflectivity upwelling and the flow field.

The boundary layer east of the dryline contains transverse rolls that propagate from south to north (Fig. 4). The transverse rolls move rather uniformly from 190 degrees at a speed of around 15 m s^{-1} , or nearly the speed of the mean low-level flow. The rolls develop and propagate along the interface between the shallow internal boundary layer and the elevated residual layer (ERL). Enhanced vertical vorticity is collocated with the roll updrafts, suggesting a vorticity growth

mechanism proceeding from the tilting of ambient BL shear and subsequent stretching amplification. Since the dryline is a zone of enhanced horizontal wind shear and vertical vorticity, the updrafts associated with individual rolls may stretch this pre-existing vorticity.

Numerous 1-3 km scale misocyclone vortices are contained in the boundary layer, with the highest concentration along or very near the dryline (Fig 3). The vorticity values in the stronger misocyclones range from 3 to greater than $6 \times 10^{-3} \text{ s}^{-1}$, or nearly the same order of magnitude as thunderstorm mesocyclones. Although determining the origin of these vortices is beyond the scope of this work, the data suggest that tilting and stretching of pre-existing horizontal vorticity may be of primary importance. Similar to the transverse rolls and dryline waves, these vortices also tend to move through the boundary layer with the mean low-level flow. Both the dryline waves and misocyclones display temporal and spatial continuity in animation of the 3-minute interval analyses (not shown). This is significant since each radar analysis is independent of each other so continuity of features is not an artifact of data sampling.

c. *Mobile Mesonet observations*

The mobile mesonets typically measured across-dryline mixing ratio gradients of order $3\text{-}4 \text{ g kg}^{-1} \text{ km}^{-1}$ (Fig. 5), similar to measured values reported by Ziegler and Rasmussen (1998) and Pietrycha and Rasmussen (2004). The west-east dryline profiles (i.e. from dry to moist) measured by the mobile mesonets are classifiable into three distinct categories, or types. The first type is characterized by a single steep “step-like” moisture rise over about 1 km, (eg. 0021-0030 traverse in fig 5c). The second type is characterized by two distinct “steps” in the moisture field (e.g. P9, 2205-2214) and is also known as the “double dryline” (Hane et al 1993; Hane et al 2001). These dryline profiles are analogous to the type 2 profiles measured by the P-3 and King Air (Demos et al 2005). The third type is characterized by a sudden moisture rise followed by a sudden drop then another sudden rise on the moist side of the dryline (e.g. P1, 2340-2359). The amplitude of the intermediate moisture drop varies from transect to transect. It is speculated that the step-like dryline profiles can be explained by horizontal and vertical transport and the local state of mixing (Ziegler and Hane 1993) within the evolving dryline secondary circulation.

The virtual potential temperature (q_v) profile is typified by higher values on the dry side than on the

moist side of the classic Type 1 one step dryline with a local maximum residing in the moisture gradient (Figs 9b, c, d, and f). Typical across-dryline q_v gradients are about 0.25 K km^{-1} , with absolute differences between 0.5 and 2 K. The nature of the local q_v maximum along the dryline varies from relative (Fig. 9d) to absolute (Figs. 6b,c, and f) and is a consequence of the relative changes in q and q_v . Type 2 and Type 3 profiles (Fig. 6e and Fig 6a respectively) have similar local temperature maxima on the moist side of the moisture gradients, although both types have local temperature minima associated with local q_v minima in the broader moisture gradient. The local q_v maxima are reflective of the moisture effect on virtual temperature for small potential temperature changes at the leading edge of the dryline. Collocation of local moisture and temperature minima (Fig. 6a, 6e) may indicate flushing by local downdrafts give the presence of an unstably stratified lower BL in which q_v decreases with height (Fig. 3). Local q_v maxima around the dryline may be important thermodynamically since these parcels will be more potentially buoyant than surrounding surface layer parcels. To the extent that the surface q_v gradient correlates with the mean BL thermal gradient, the existence and location of local temperature maxima will determine if the solenoidally forced updraft will primarily lift dry or moist surface layer air.

Mobile mesonet wind measurements typically indicate south to southeasterly winds to the east of the dryline with west to southwest winds to the west of the dryline, and the main confluence zone is collocated with the strongest moisture gradient (Figs. 6b,c,d,f). Two of the dryline transects indicate sharp local drying and cooling the mesonets concurrent with a rapid backing of the winds to the northeast (Fig. 6a,e), although the main confluence band is associated with the westernmost q_v and q_v gradients. The wind profiles associated with these “dry pockets” may indicate that they were produced by vortices propagating along the dryline.

d. *Mobile Sounding data*

Horizontal gradients of boundary layer stratification are revealed by the mobile sounding array (Fig. 2). West of the dryline the hot, dry convective boundary layer BL is more than 300 mb deep with a nearly constant well mixed potential temperature and a slight decrease in mixing ratio with height (Fig 2b). The CBL is capped by a warm dry layer around 600 mb (3.4 km AGL), approximately the LCL for a lowest 50 mb mixed parcel. West of the dryline the winds are

strong out of the south-southwest near the surface, veering slightly to southwest near the top of the CBL, subsequently veering to the west-southwest above the CBL. The sounding to the west of the secondary dryline (Fig. 2a) is drier conditions through the CBL. Between the primary and secondary drylines, the water vapor mixing ratio remains nearly constant between 750 and 600 mb, whereas to the west the CBL this layer dried off rapidly with height (Fig 2b vs. 2a). East of the dryline the lowest 750 m are relatively cool and moist with an LCL of 2.1 km (Fig. 2c). This shallow moist internal boundary layer is capped by a warm, dry ERL as the CBL to the west is advected up and over the surface dryline. Thus, above the moist internal boundary layer the sounding east of the dryline (Fig. 3c) is almost identical in temperature and only slightly moister than the sounding west of the dryline (Fig. 2b).

e. *GOES-8 satellite analyses*

Brightness data obtained from the GOES-8 satellite were analyzed on the radar grid for 2327 and 2345 (Fig. 7). At 2327 there are five main areas of cloud, three of which are along and just east of the dryline, one west of the dryline along an HCR, and one along the secondary dryline. In general these cloud features are associated with updraft cores at the 1.5 km level. At 2345 as the dryline circulation intensifies, nearly all the associated clouds have become oriented along a band of higher vertical velocities at the dryline. Animated gridded GOES-8 imagery (not shown) reveal cloud areas moving from south to north across the domain and substantially evolving over a short (~10 min) period of time.

f. *Thermodynamic analyses*

Fields of surface water vapor mixing ratio illustrate the Lagrangian analysis and reveal aspects of dryline evolution (Fig. 8). The dryline is revealed as a sharply defined gradient in q_v residing in a narrow zone of confluence. The gradients reproduced by these analyses have a degree of spatial and temporal variability but are generally on the order of $2\text{-}3 \text{ g kg}^{-1} \text{ km}^{-1}$, approximately the magnitude measured along each of the individual mobile mesonet dryline crossing transects (Fig. 5). The nature of the analysis is such that the technique reproduces gradients, which form through frontogenesis, that are advected upstream and downstream. In addition to the strong gradients, smaller scale along line variability is noted along the dryline. For example, vortices that form and move along the dryline locally alter the structure of the

moisture gradient (see Fig. 13a,b) . North of a vortex the associated tangential velocity advects moisture westward whereas south of the vortex moisture advects eastward. Due to the relative magnitude of the tangential velocity associated with the vortex and the speed of the low level flow, the resulting moisture field near the vortex takes the form of a low amplitude wave (e.g. Fig. 8b-c). Results to be shown later will reveal that a particularly strong mesocyclone is associated with a wave in the moisture field and has temporal continuity. Later in the period, portions of the dryline develop an “S” profile featuring a band of drier air residing between the moist BL and a moist tongue to the west. In these regions the strongest confluence is located along the western moisture gradient suggesting, that the segmentation is a result of entrainment to the east of the westernmost surface dryline (eg. the 2344-2359 P1 traverse Fig. 9b).

The Lagrangian analysis resolves the secondary dryline west of the primary dryline (Fig 8a) early in the analysis period. As is the primary dryline this feature is characterized by a moisture gradient within a confluence band. Unlike the primary dryline, the moisture gradient associated with the secondary dryline is much smaller (i.e. $\sim 1\text{-}2 \text{ g kg}^{-1} \text{ km}^{-1}$). Fewer details in the structure of the secondary dryline can be gleaned from this analysis however, as it was only sampled by one mobile mesonet.

The motion of the dryline as a whole is tracked via isochrones of the dryline position determined from the water vapor mixing ratio analyses performed at 9-minute intervals from 2242-0012 (Fig. 9). At 2242 and 2251 the dryline is located just west of X-pol and Homestead and is moving very slowly westward, but by 2300 the dryline has moved rapidly westward by several kilometers and remains nearly stationary until the 2327 analysis. After 2329, the dryline moves eastward and is located at nearly the same position as it was at 2242 and 2251. From 2327 through 2345, the dryline again moves westward before accelerating its retrogression between 2345 and 2354. From 2354 through 0012 the dryline continues its retrogression at varying speeds.

In the vertical the dryline is characterized by the transition zone between the deep dry CBL to the west and the shallow moist layer to the east. The shallow moist layer is capped by the dry CBL air that is advected up and over the dryline from the west. The depth of the moist layer varies depending on the structure of the circulations and attendant vertical motions within the layer.

The most striking feature of the dryline-normal vertical dryline structure (Fig. 10) is the strong secondary circulation at the dryline. This vertical circulation and enhanced convergence inferred to be forced by solenoids in previous studies (e.g. Parsons et al 1991; Ziegler et al 1995), results in maximum vertical velocity around the dryline location. These strong updrafts act to lift moisture at the head of the dryline resulting in a local deepening of the moist layer. Due to the relative magnitude of the westerly shear above the dryline to the strength of the updraft, moisture can be advected out of the updraft resulting in an elevated moist layer east of the dryline (see Fig. 10b). Additionally, the depth of the moist layer may be modulated by interactions with the structures in the ERL. Deeper moisture bands are oriented along the mean ERL flow, possibly induced by the ascending branch of HCRs that are lifted up and over the dryline, with clockwise deflection due to the solenoidal vertical shear. The secondary dryline circulation is locally strong enough to advect dry air from the ERL nearly to the surface. It is speculated that downward transport of dry air in concert with subgrid-scale vertical mixing generates the segmented dryline structure described in section 3c.

Relatively moist (dry) air is associated with relatively cool (warm) q_v in the BL (Fig. 11). The q_v east of the dryline is fairly shallow and is capped by the warm CBL air advected up and over the dryline. As with moisture, the depth and structure of the q_v fields east of the dryline are modulated by the circulations and vertical motions within the moist layer. The structure of the q_v (and therefore density) gradients are important, as they provide the forcing for the solenoidal secondary circulation at the dryline. As the dryline circulation strengthens, a mixture of air from both sides of the dryline is lofted by the updrafts. Since it is hypothesized that to form a cloud air must reach its LCL before detraining from the updraft, the westerly shear at the dryline necessitates a strong, deep updraft to form a cloud in rising air with a lower saturation point (SP). Although observed cloud bases were above the 2.5 km domain, clouds were observed by both the GOES-8 satellite and CAM-1. The lifting of relatively low-SP air leads to a rapid increase in relative humidity with height within the updraft. Extrapolating the increase in relative humidity with height above the domain implies that the LCL would be reached at about 2.8 km AGL. This is approximately the mean LCL height calculated from the soundings just east (2.1 km)

and west (3.4 km) of the dryline, indicating that the air within the dryline updraft is a mixture of the two airmasses.

4. DISCUSSION

a. *Dryline frontogenesis*

The horizontal frontogenesis function of q_v is calculated to diagnose regions where gradients in moisture are being created or dissipated along the dryline (not shown). The surface dryline is primarily frontogenetic along its entire length, except for a few spots of very weak frontolysis. Along-dryline gradients are advected and also strengthened in the downstream direction, since airflow trajectories are nearly parallel to the dryline and thus experience confluent forcing over residence times within the dryline zone. The secondary dryline is also frontogenetic, but the magnitude is generally less than that of the primary dryline due to the weaker confluence and moisture gradient.

The dryline zone exhibits frontogenesis at low levels and frontolysis at higher levels. This frontogenesis pattern is indicative of strong convergence in the lower part and divergence in the upper part of the boundary layer along the dryline (Ziegler et al 1995). As air is lifted in the updraft, the strong secondary dryline circulation acts to transform the large horizontal gradients of moisture into vertical gradients. This process of lifting and rotating surface horizontal gradients is frontolytic in the 2-D horizontal planes in which the frontogenesis function is calculated. The structure of the frontogenesis along the secondary dryline is similar to that along the primary dryline, with frontogenesis (frontolysis) at lower (upper) levels of the boundary layer.

d. *Dryline vortices*

Pietrycha and Rasmussen (2004) showed several cases where small-scale vortices were observed to track and augment the moisture gradients along the dryline, with similar vortex-dryline interactions noted in the present case. In series of radar analyses presented in a reference frame following the motion of a single misocyclone dryline vortex, a wave moves northward along the dryline with the misocyclone remaining located near its inflection point (Fig. 12). The vortex location also corresponds to the intersection of the dryline with a longitudinal HCR extending upstream into the dry air. Both the dryline and the misocyclone, the latter with a maximum vertical

vorticity on the order of $9 \times 10^{-3} \text{ s}^{-1}$, show surprisingly little evolution over 9 minutes.

North of the misocyclone, the westward acceleration of the winds retrogrades the dryline and induces a deformation zone in the flow field, thereby enhancing vertical motion. To the south of the misocyclone, the vortex induced flow is accelerated eastward and enhances convergence along a newly formed dryline section east of its previous location. As the misocyclone develops, it rotates a segment of the dryline counter-clockwise from a north-south to east-west orientation and thereby creating the wave's inflection. The reflectivity structure follows a similar pattern to that of the vertical velocity as the boundary layer scatterers are being displaced (Fig. 13c,d). Near the surface the highest reflectivities are located below the strongest upward vertical motion at 750 m AGL, both along the dryline and along the HCR extending to the southwest. As the vortex moves northward along the dryline, moisture is scoured to its south as increasing westerly momentum advects dry air from the west, thereby decreasing the depth of the moist layer. Just after vortex passage a new gradient in moisture begins to form to the east in the area of strongest convergence and frontogenesis. To the west, at the old location of the dryline, a gradient in moisture is still seen, thus leading to a "double dryline" structure.

The tightening gradient along the eastern dryline locally veers the winds within the "double dryline" zone, a frontolytic situation develops along the old dryline location. Combined with continued vertical mixing of the shallow moisture, frontolysis eventually dissipates the old dryline south of the vortex. North of the vortex, an easterly component of the wind develops which transports moisture horizontally, thereby locally deepening the moist layer. Moisture is somewhat shallower through the center of the vortex where little in the way of advection is acting on the moisture field. To the south of the vortex the strong westerly momentum brings dry air eastward and, combined with vertical mixing, rapidly decreases the depth of the moist layer. Continued mixing farther to the south (relative to the vortex) eventually leads to the complete dissipation of the dryline at its previous position to be replaced with its new, more easterly position.

5. CONCLUSIONS

This paper presents Lagrangian analysis of the 3-D the structure and evolution of the dryline and the surrounding BL on 22 May 2002 using mobile ground-based radar and in-situ data obtained during the IHOP field project. Using the time-varying 3D wind fields, trajectories are computed from the in situ mesonet, aircraft, and grid point pseudo-sounding data locations. The observed q_v , q , and q_v data are then advected along trajectories and objectively analyzed to the grid using a 2-pass Barnes scheme, weighting both in space and time. Inferences of the processes of dryline formation and movement and cloud development are facilitated by these kinematic and Lagrangian BL analyses.

From a radar perspective, the dryline is characterized by a nearly north-south oriented band of enhanced reflectivity and vertical velocity residing in a zone of confluence. In the vertical, the winds within the shallow (~ 750 m deep) moist internal boundary layer have a relative easterly component, whereas in the deep dry boundary layer the winds have a relative westerly component. At the vertical interface between these two airmasses, a strong solenoidally forced circulation persists and acts to lift the dry air to the west up and over the dryline. A secondary dryline is located farther to the northwest of the primary dryline and exhibits similar features, though less pronounced. The dryline and surrounding CBL change structure during the nearly 2-hour analyses period. Initially, the dryline is nearly stationary and convection in the CBL west of the dryline exhibits a complex structure of open cellular and banded features. As longitudinal bands, or HCRs, eventually become the dominant convective mode west of the dryline, transverse rolls develop to the east. Concurrent with the surrounding CBL organization, strong vortices and associated dryline waves develop near the intersections of the dryline with HCRs. As surface heating decreases, the BL convection west of the dryline becomes more disorganized, the smaller scale vortices are replaced with larger scale (~ 15 km) waves, and the dryline retrogrades to the west.

Mobile mesonet transects provide the majority of the thermodynamic information that goes into the analyses and due to the analysis techniques show more structure in the along-leg gradients than the final analyses. From the 1 Hz data we see typical across-dryline gradients of q_v and q are typically of order $2\text{--}4$ $\text{g kg}^{-1} \text{ km}^{-1}$ and 0.25 K km^{-1} respectively. Several distinct profiles are seen in the individual mobile mesonet dryline crossing traverses. The moisture

profile is typically characterized by nearly constant values on either of the dryline with single or multiple sharp “step-like” drops in moisture across the dryline, although localized moisture minima are occasionally observed which indicate inflection of the dryline not previously reported. The variations in the moisture profiles are most likely caused by the interactions of the vortices with the dryline.

The Lagrangian thermodynamic analysis reveals that the q_v and q gradients reside within or very near the confluence zone noted in the wind fields. The vertical structure of the dryline is characterized by a cool, moist internal boundary layer capped by the deep hot, dry CBL, which advects up and over the dryline from the west. In the lower levels convergence along the dryline is frontogenetic and acts to produce and maintain the q_v and q gradients, whereas in the upper levels of the CBL the circulation is divergent and frontolytic, tilting the horizontal gradients into the vertical. The secondary circulation along the dryline gradient also acts to lift both moist and dry parcels upward. Depending on the amount of moist or dry air lifted, along with the actual properties of that air, areas within certain updrafts will be closer to saturation than others. Although the maximum relative humidity reached in the analyses was only around 60%, from the change in humidity along a trajectory extrapolation out of the analysis domain gives an estimate of approximately where clouds should be located assuming they remained within an updraft to their LCL above the top of our domain. These locations compare well subjectively with locations of clouds obtained from the satellite brightness data.

Coherent airflow features are observed which imply a level of predictability in the BL. One such feature noted in this study are the small-scale vortices which propagated from south to north along the dryline. The strongest vortices are persistent and can be tracked through nearly the entire analysis domain (30 km) for upwards of 30 minutes in time. Over a 9 minute period spanning 4 radar analyses, the strongest misocyclone shows surprisingly little evolution. As the vortices move along the dryline, their airflow perturbations augment the dryline’s thermodynamic structure. North of the vortex, the moist internal boundary layer is deepened as moist air is brought westward and lifted at the dryline. South of the vortex, strong westerly momentum transports dry air to the east, thereby scouring moisture from top down and decreasing the moist layer depth. Further vertical mixing and transport effectively dissipate the dryline at its previous location

while frontogenetical forcing produces a new dryline gradient several kilometers to the east. Therefore, the procession of vortices from south to north acts to continuously force the dryline eastward via their passage. The vortices are collocated with sustained updrafts, suggesting they promote lifting of moist air to the local LCL and implying that a tilting/stretching mechanism may be responsible for mesocyclone formation.

6. ACKNOWLEDGEMENTS

The authors would like to thank Bob Rabin for his help with the renavigation and display of the GOES-8 satellite data. We acknowledge the assistance of Dick Oye and Jay Miller with the NCAR Solo, Reorder, and Cedric software packages. Partial funding for this research was provided by National Science Foundation (NSF) grant ATM-013016. Funding for DOW radar deployment was provided under NSF grant ATM-0208651.

7. REFERENCES

- Arnott, N. R., Y. P. Richardson, J. M. Wurman, and J. Lutz, 2003: A solar alignment technique for determining mobile radar pointing angles. Preprints, 31st International Conference on Radar Meteorology, Seattle, WA, Amer. Meteor. Soc., 492-494.
- Atkins, N. T., R. M. Wakimoto, and C. L. Ziegler, 1998: Observations of the finescale structure of the dryline during VORTEX 95. *Mon. Wea. Rev.* **126**, 525-549.
- Bean, B. R., and Dutton E. J., 1968: Radio Meteorology. National Bureau of Standards Monogr., No. 92, National Bureau of Standards, 435 pp.
- Biggerstaff, Michael I., and Jerry Guynes, 2000: A new tool for atmospheric research. Preprints, 20th Conference on Severe Local Storms, Orlando, FL, Amer. Meteor. Soc., 277-280.
- Biggerstaff, M., L. Wicker, J. Guynes, C. Ziegler, J. Straka, E. Rasmussen, A. Doggett, IV, L. Carey, and J. Schroeder, 2005: The Shared Mobile Atmospheric Research and Teaching (SMART) radar: A collaboration to enhance research and teaching. *Bull. Amer. Meteor. Soc.*, **86**, [in press].
- Bluestein, H. B., E. W. McCaul Jr., G. P. Byrd and G. R. Woodall. 1988: Mobile Sounding Observations of a Tornadoic Storm near the Dryline: The Canadian, Texas Storm of 7 May 1986. *Monthly Weather Review*: Vol. 116, No. 9, pp. 1790-1804.
- Bluestein, H. B., and S. S. Parker. 1993: Modes of Isolated, Severe Convective Storm Formation along the Dryline. *Monthly Weather Review*: Vol. 121, No. 5, pp. 1354-1372.
- Bluestein, H. B., 1993: Synoptic-Dynamic Meteorology in Midlatitudes. Vol. 2, Observations and Theory of Weather Systems. Oxford University Press, 594 pp.
- Carbone, R.E., 1982: A Severe Frontal Rainband. Part I. Stormwide Hydrodynamic Structure. *Journal of the Atmospheric Sciences*: Vol. 39, No. 2, pp. 258-279.
- Demoz, B., C. Flamant, D. Miller, K. Evens, F. Fabry, P. Girolamo, D. Whiteman, B. Geerts, T. Weckwerth, W. Brown, G. Schwemmer, B. Gentry, W. Feltz, and Z. Wang, 2005: Dryline on 22 May 2002 during IHOP: Convective scale measurements at the profiling site. *Mon. Wea. Rev.* In press.
- Hane, C. E., C. L. Ziegler and H. B. Bluestein. 1993: Investigation of the Dryline and Convective Storms Initiated along the Dryline: Field Experiments during COPS-91. *Bull. Amer. Meteor. Soc.*, Vol. 74, No. 11, pp. 2133-2145.
- Hane, C. E., H. B. Bluestein, T. M. Crawford, M. E. Baldwin and R. M. Rabin. 1997: Severe Thunderstorm Development in Relation to Along-Dryline Variability: A Case Study. *Mon. Wea. Rev.*, Vol. 125, No. 2, pp. 231-251.
- Hane, C. E., M. E. Baldwin, H. B. Bluestein, T. M. Crawford and R. M. Rabin. 2001: A Case Study of Severe Storm Development along a Dryline within a Synoptically Active Environment. Part I: Dryline Motion and an Eta Model Forecast. *Mon. Wea. Rev.*, Vol. 129, No. 9, pp. 2183-2204.
- Johns, R. H., and C. A. Doswell III. 1992: Severe Local Storms Forecasting. *Weather and Forecasting*: Vol. 7, No. 4, pp. 588-612.

- Kingsmill, D. E., 1995: Convection Initiation Associated with a Sea-Breeze Front, a Gust Front, and Their Collision. *Monthly Weather Review*: Vol. 123, No. 10, pp. 2913–2933.
- Koch, S. E., 1979: Mesoscale gravity waves as a possible trigger of severe convection along a dryline. Ph.D. dissertation, University of Oklahoma, Norman.
- Koch, S., M. DesJardins, and P. Kocin, 1983: An interactive Barnes objective map analysis scheme for use with satellite and conventional data. *J. Climate Appl. Meteor.*, 22, 1487–1503.
- Laird, N.F., D. A.R. Kristovich, R. M. Rauber, H. T. Ochs III and L. J. Miller. 1995: The Cape Canaveral Sea and River Breezes: Kinematic Structure and Convective Initiation. *Monthly Weather Review*: Vol. 123, No. 10, pp. 2942–2956.
- Mahoney, W. P. III., 1988: Gust Front Characteristics and the Kinematics Associated with Interacting Thunderstorm Outflows. *Monthly Weather Review*: Vol. 116, No. 7, pp. 1474–1492.
- McCarthy, J., and S. E. Koch, 1982: The evolution of an Oklahoma dryline. Part I: A meso- and subsynoptic-scale analysis. *J. Atmos. Sci.*, 39, 225–236.
- McNulty, R. P., 1995: Severe and Convective Weather: A Central Region Forecasting Challenge. *Weather and Forecasting*: Vol. 10, No. 2, pp. 187–202.
- Mohr, C. G., L. J. Miller, R. L. Vaughan, and H. W. Frank, 1986: The merger of mesoscale datasets into a common Cartesian format for efficient and systematic analyses. *J. Atmos. Oceanic. Technol.*, 3, 144–161.
- Nielsen, J. W., and P. P. Neill. 1990: The Vertical Structure of New England Coastal Fronts. *Monthly Weather Review*: Vol. 118, No. 9, pp. 1793–1807.
- Oye, R., C. Mueller, and S. Smith, 1995: Software for radar translation, visualization, editing, and interpolation. *Preprints, 27th Conf. on Radar Meteorology*, Vail, CO, Amer. Meteor. Soc., 359–361.
- Parsons, D. B., M. A. Shapiro, R. M. Hardesty, R. J. Zamora and J. M. Intrieri. 1991: The Finescale Structure of a West Texas Dryline. *Monthly Weather Review*: Vol. 119, No. 5, pp. 1242–1258.
- Pietrycha, A. E., and E. N. Rasmussen. 2004: Finescale Surface Observations of the Dryline: A Mobile Mesonet Perspective. *Weather and Forecasting*: Vol. 19, No. 6, pp. 1075–1088.
- Rasmussen, N. E., R. Davies-Jones, C. A. Doswell Jr., F. H. Carr, M. D. Eilts, D. R. MacGorman, J.M. Straka and F. H. Carr. 1994: Verification of the Origins of Rotation in Tornadoes Experiment: VORTEX. *Bulletin of the American Meteorological Society*: Vol. 75, No. 6, pp. 995–1006.
- Rhea, J. O., 1966: A study of thunderstorm formation along drylines. *J. Appl. Meteor.*, 5, 58–63.
- Rust, W. D., R. P. Davies-Jones, D. W. Burgess, R. A. Maddox, L. C. Showell, T. C. Marshall, and D. K. Lauritsen, 1990: Testing a mobile version of a cross-chain Loran atmospheric sounding system (M-CLASS). *Bull. Amer. Meteor. Soc.*, 71, 173–180.
- Schaefer, J.T., 1974: A Simulative Model of Dryline Motion. *Journal of the Atmospheric Sciences*: Vol. 31, No. 4, pp. 956–964.
- Straka, J. M., E. N. Rasmussen, and S. E. Fredrickson, 1996: A mobile mesonet for fine scale meteorological observations. *J. Atmos. Oceanic Technol.*, 13, 921–936.
- Sun, W. and C. Wu. 1992: Formation and Diurnal Variation of the Dryline. *Journal of the Atmospheric Sciences*: Vol. 49, No. 17, pp. 1606–1619.
- Wakimoto, R. M., 1982: The Life Cycle of Thunderstorm Gust Fronts as Viewed with Doppler Radar and Rawinsonde Data. *Monthly Weather Review*: Vol. 110, No. 8, pp. 1060–1082.
- Weckwerth, T. M., D. B. Parsons, S. E. Koch, J. A. Moore, M.A. LeMone, B. B. Demoz, C. Flamant, B. Geerts, J. Wang and W. F. Feltz. 2004: An Overview of the International H2O Project (IHOP_2002) and Some Preliminary Highlights. *Bulletin of the American Meteorological Society*: Vol. 85, No. 2, pp. 253–277.
- Weckwerth, T. M., and D. B. Parsons, 2005: A review of convection initiation and motivation for IHOP_2002. *Mon. Wea. Rev.* In press.

- Weckwerth, T. M., C. R. Pettet, F. Fabry, S. Park, M. A. LeMone and J. W. Wilson. 2005: Radar Refractivity Retrieval: Validation and Application to Short-Term Forecasting. *Journal of Applied Meteorology*: Vol. 44, No. 3, pp. 285–300.
- Weiss, C. C. and H. B. Bluestein. 2002: Airborne Pseudo–Dual Doppler Analysis of a Dryline–Outflow Boundary Intersection. *Mon. Wea. Rev.*, Vol. 130, No. 5, pp. 1207–1226.
- Weiss, C. C., H. B. Bluestein, and A. L. Pazmany. 2005: Fine-scale Radar Observations of the 22 May 2002 Dryline During the International H₂O Project (IHOP). *Mon. Wea. Rev.* [In review]
- Wurman, J., J. Straka, E. Rasmussen, M. Randall, and A. Zahrai, 1997: Design and deployment of a portable, pencil-beam, pulsed, 3-cm Doppler radar. *J. Atmos. Oceanic Technol.*, 14, 1502-1512.
- Wurman, 2001: The DOW mobile multiple Doppler network. Preprints, 30th International Conference on Radar Meteorology, Munich, Germany, Amer. Meteor. Soc., 95-97.
- Ziegler, C.L., and C. E. Hane, 1993: An observational study of the dryline. *Mon. Wea. Rev.* **121**, 1489-1506.
- Ziegler, C. L., W. J. Martin, R. A. Pielke and R. L. Walko. 1995: A Modeling Study of the Dryline. *J. Atmos. Sci.* Vol. 52, No. 2, pp. 263–285.
- Ziegler, C. L., T. J. Lee, and R. A. Pielke Sr.. 1997: Convective Initiation at the Dryline: A Modeling Study. *Mon. Wea. Rev.* Vol. 125, No. 6, pp. 1001–1026.
- Ziegler, C. L., and E. N. Rasmussen, 1998: The initiation of moist convection at the dryline: Forecasting issues from a case study perspective. *Wea. For.*, 13, 1106-1131.
- Ziegler, C. L., D. Kennedy, and E. N. Rasmussen, 2004: A mobile mesonet for fine scale meteorological observations. *J. Atmos. Oceanic Technol.*, 21, 1659-1669.
- Ziegler, C. L., M. S. Buban, and E. N. Rasmussen, 2005: A Lagrangian thermodynamic analysis technique for assimilating in-situ observations in multiple radar-derived airflow. *Mon. Wea. Rev.*, [in review]

Radar specifications	SR-1	DOW-2	DOW-3	X-Pol
Beam width (km)	1.5	.95	.95	.95
Gate spacing (m)	67	75	75	210
Volume scan rate (min)	2.0	1.3	1.3	1.3
Scan volume spacing (min)	3	1.5	1.5	1.5

Table 1. Radar specifications for the four mobile Doppler radars participating in the data collection on 22 May 2002.

Analysis interval	SR-1	DOW-2	DOW-3	X-Pol	Total radars
2233-2251		x	x	x	3
2254-2257	x	x	x	x	4
2300-2312	x	x	x		3
2315	x	x	x	x	4
2318-2342	x	x	x		3
2345-2351	x	x	x	x	4
2354-0012	x	x	x		3
0015	x	x	x	x	4
0018-0024	x	x	x		3

Table 2. Participating mobile Doppler radars during various analysis time periods from 2233-0024 on 22 May 2002. Data were collected by at least one radar between 2230 and 0100.

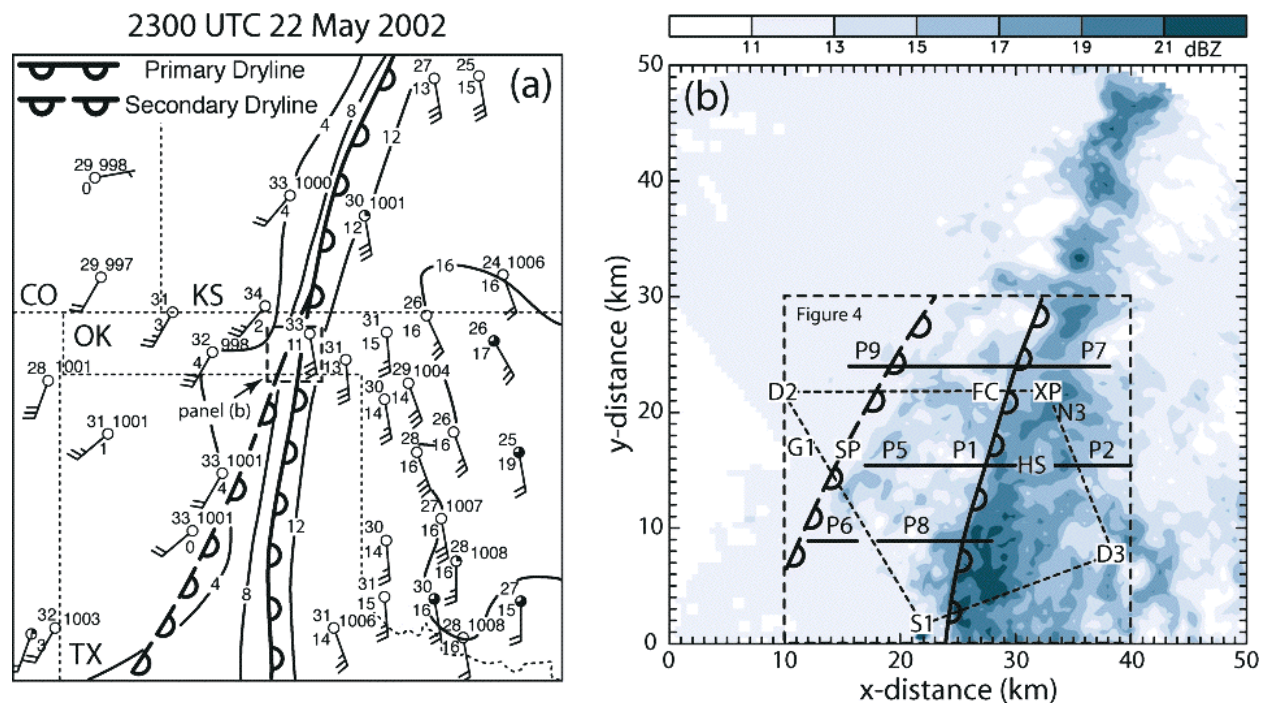


Figure 1. Surface conditions on 22 May 2002 at 2300 UTC. (a) Surface map with standard station models and subjectively analyzed dewpoint (solid black lines) ($^{\circ}\text{C}$). (b) Radar reflectivity (dBZ) in the radar analysis domain including the locations of the radars and mobile mesonet legs. The location of the radar analysis domain is shown by the dashed box in panel (a). The black dashed box in panel (b) is the thermodynamic analysis domain. In both panels, the locations of the primary dryline (solid line with semicircles) and secondary dryline (dashed line with semicircles) are shown.

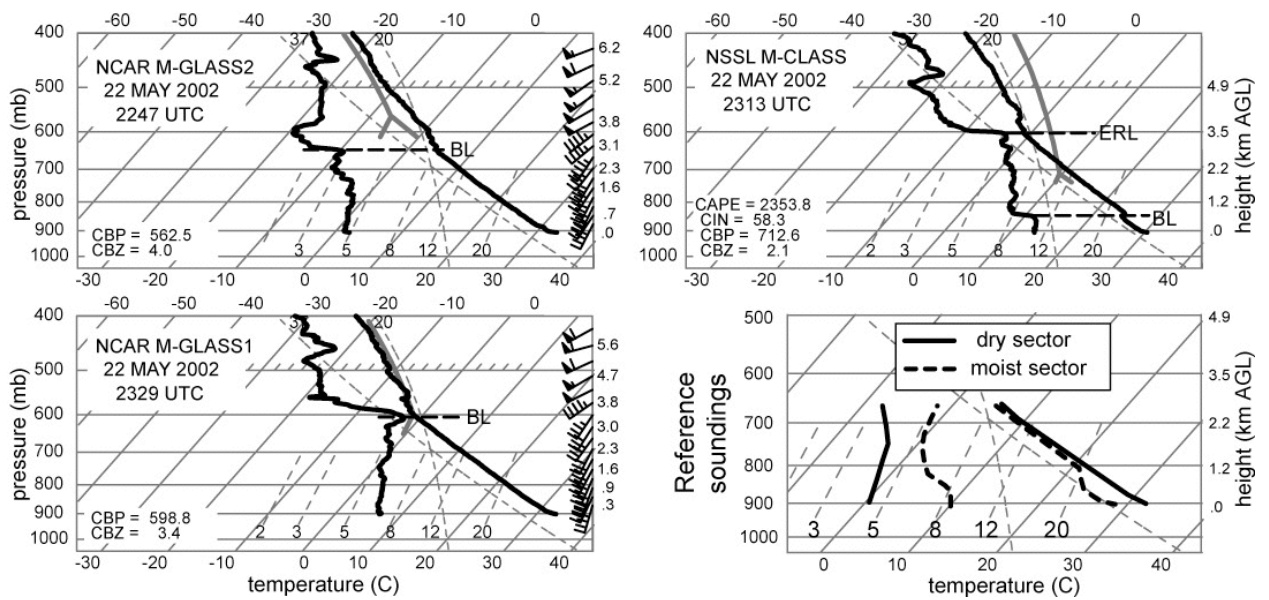


Figure 2. Mobile soundings launched on 22 May 2002. (a) 2247 NCAR GLASS sounding launched west of the secondary boundary; (b) NSSL CLASS sounding launched east of the dryline; (c) NCAR GLASS sounding launched east of the secondary boundary but west of the primary dryline; (d) the reference soundings derived from observed soundings and used in the Lagrangian analyses.

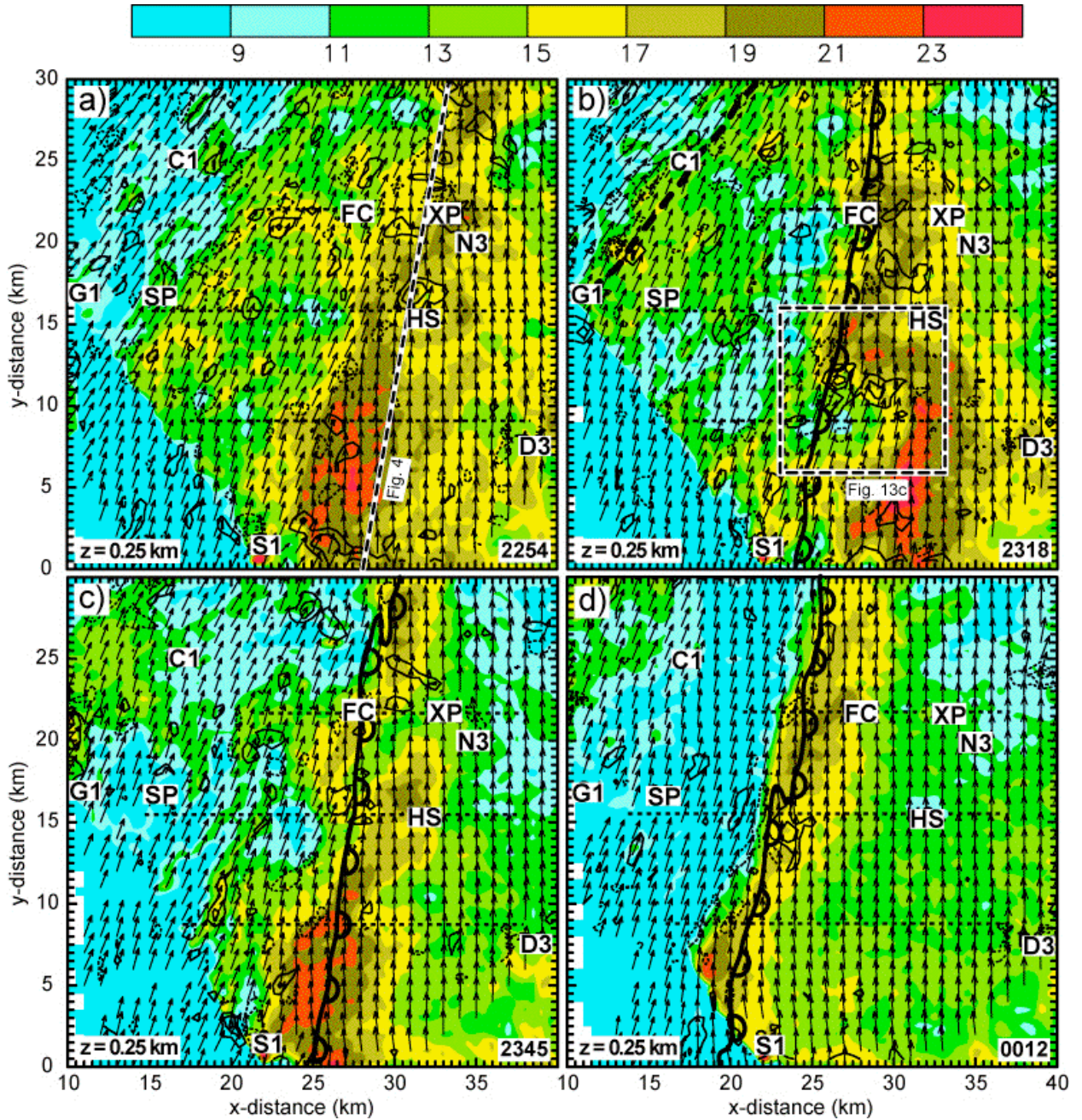


Figure 3. Radar analysis fields at 0.25 km AGL on 22 May 2002. Reflectivity (dbz), horizontal wind vectors (every other grid point with one km vector length equal to 15 m s^{-1}), and vertical vorticity (s^{-1}) every $3 \times 10^{-3} \text{ s}^{-1}$ with positive values (black solid lines) starting at $3 \times 10^{-3} \text{ s}^{-1}$ and negative values (black dotted line) starting at $-3 \times 10^{-3} \text{ s}^{-1}$. (a) 2254; (b) 2321; (c) 2348; (d) 0003. Also labeled are the locations of the Field Coordinator vehicle (FC), the digital camera operator (C1), the mobile GLASS (G1) and CLASS (N3) sounding systems, DOW-3 (D3), the SMART radar (SR1), and Homestead (HS). The thin dashed lines indicate roads being used by the mobile mesonets to collect data. The thick black nearly north-south line indicates the location of the cross-section shown in Fig. 4. The position of the dryline as determined by the thermodynamic analyses are also shown.

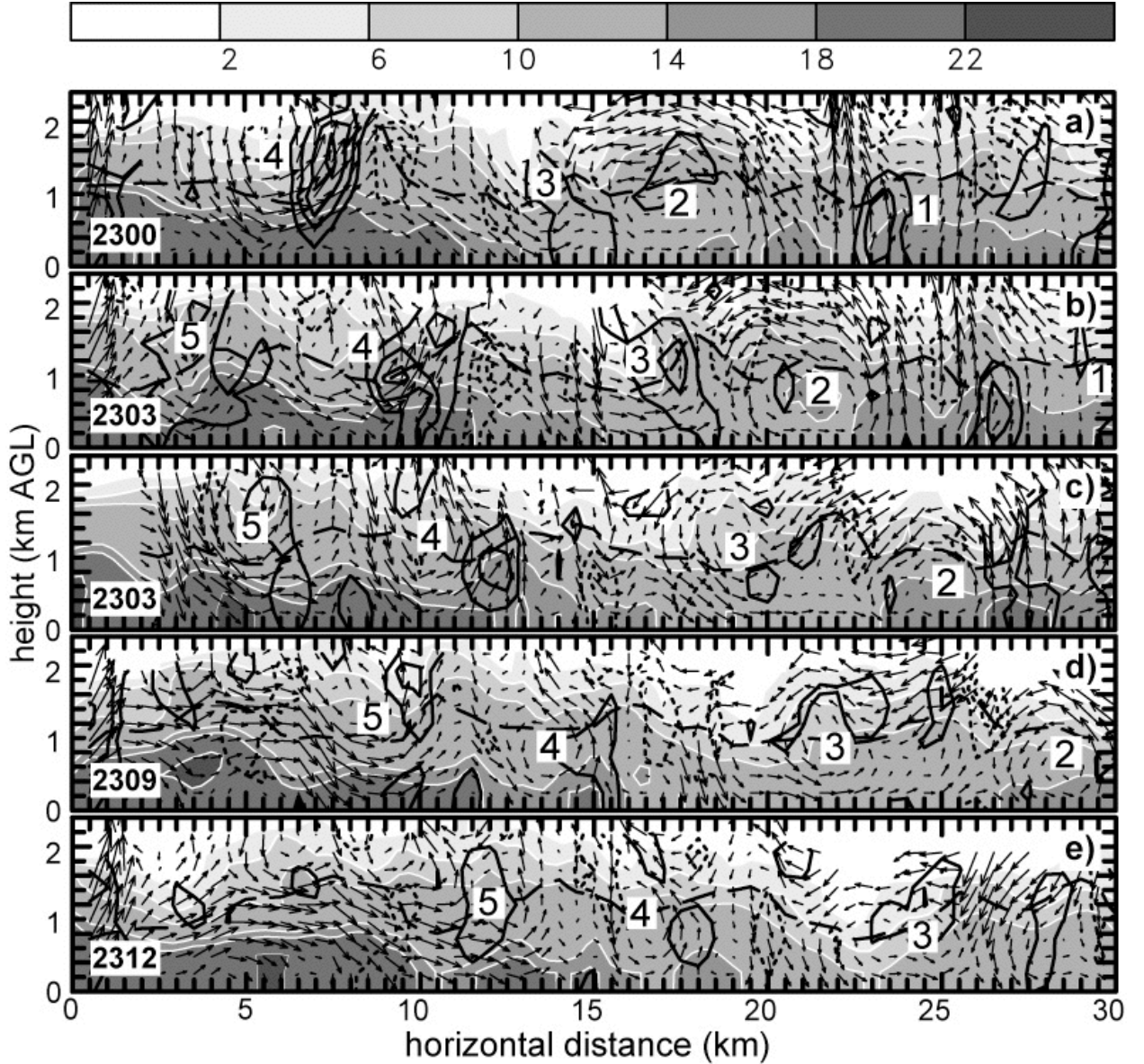


Figure 4. Vertical dryline-parallel cross-sections of reflectivity (dbz), mean wind-relative wind vectors plotted at every other grid point (with 1 km length equal to 15 m s⁻¹), and vertical vorticity (s⁻¹) every 2 x 10⁻³ s⁻¹ with positive values (black solid lines) starting at 2 x 10⁻³ s⁻¹ and negative values (black dotted line) starting at -2 x 10⁻³ s⁻¹. Above (below) the long dashed black line, the flow is greater than (less than) 5 m s⁻¹ out of the plane. The mean horizontal wind was subtracted from the wind vectors to better identify circulations. Cross-section locations are denoted by the nearly north-south oriented dashed black line in Fig. 3. Individual transverse rolls are numbered from 1 to 5 in order of appearance.

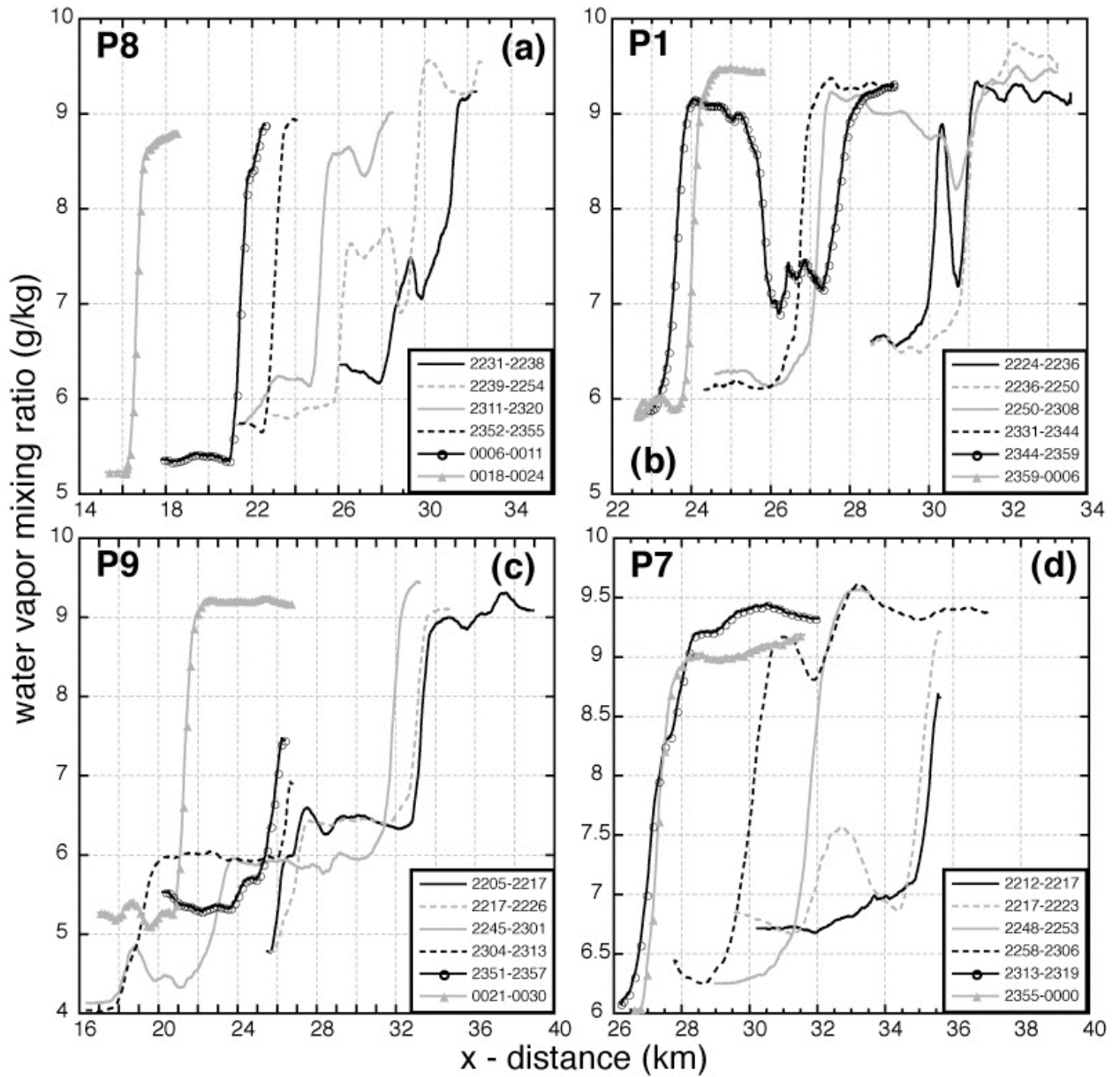


Figure 5. Mobile mesonet traverses of water vapor mixing ratio (g kg^{-1}) as a function of horizontal distance (km) in the radar analysis grid during the times indicated in the lower right hand corner from: (a) Probe 8; (b) Probe 1; (c) Probe 9; and (d) Probe 7. Probe 8 was located on the southern road, probe 1 on the center road, and Probes 9 and 7 on the northern road as depicted in Fig. 3.

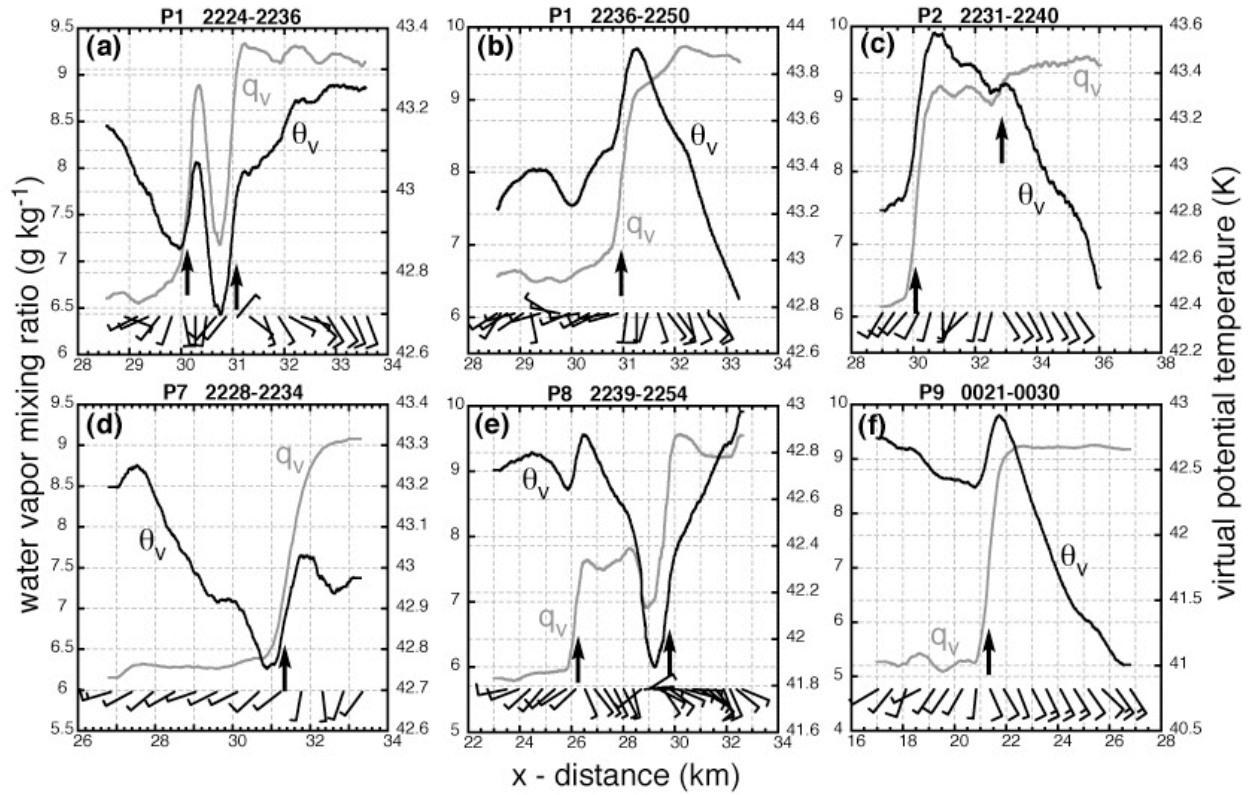


Figure 6. Water vapor mixing ratio (grey curve) and virtual potential temperature (black curve) during individual mobile mesonet dryline traverses. (a) Probe 1 from 2224-2236 UTC; (b) Probe 1 from 2236-2250 UTC; (c) Probe 2 from 2231-2240 UTC; (d) Probe 7 from 2228-2234 UTC; (e) Probe 8 from 2239-2254 UTC; and Probe 9 from 0021-0030 UTC. Relative winds (mesonet measured minus a constant wind vector) are shown below the curves with a full barb equal to 5 m s^{-1} and a half barb equal to 2.5 m s^{-1} . Arrows locate moisture gradients referred to in the text.

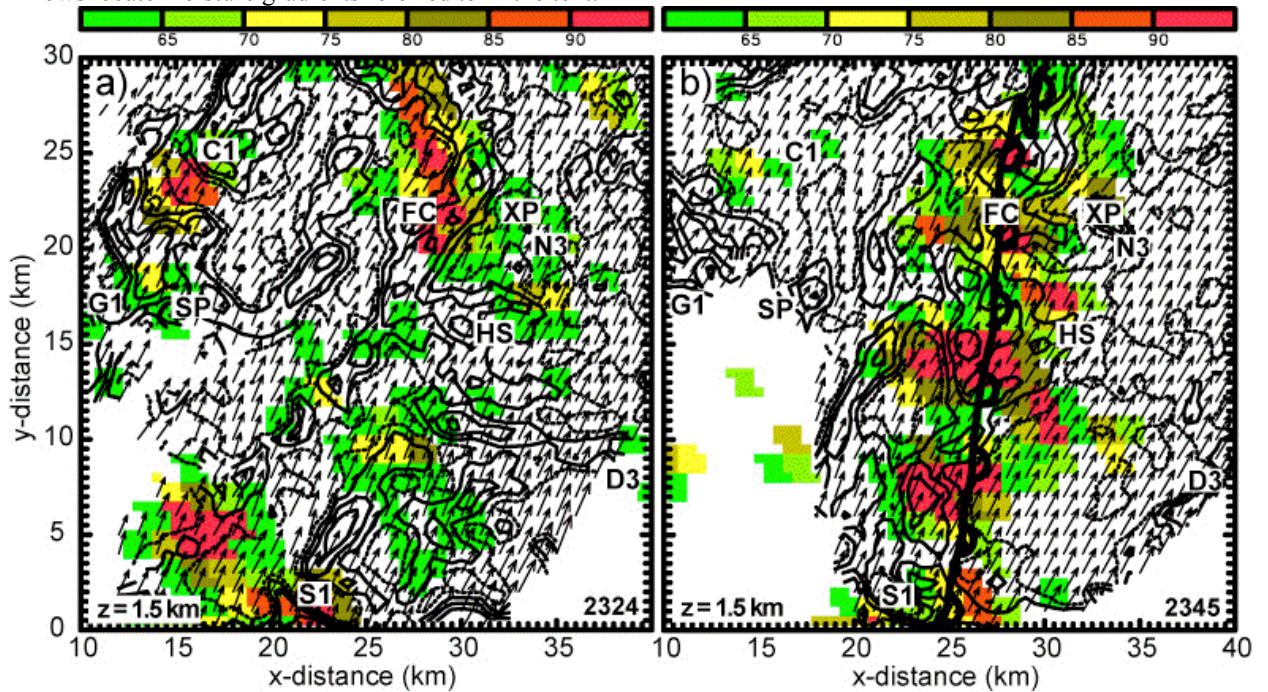


Figure 7. GOES-8 satellite images at (a) 2327 UTC and (b) 2345 UTC on 22 May 2002. Image brightness (on a scale of 0-255) color filled with warmer colors indicating higher brightness. Also shown are horizontal wind vectors (with 1 km equal to 15 m s^{-1}) and updraft (solid black lines every m s^{-1} starting at 1 m s^{-1}). The dotted black line is the 0 m s^{-1} vertical velocity contour. The location of the dryline at the 2345 UTC thermodynamic analysis time is shown in panel (b).

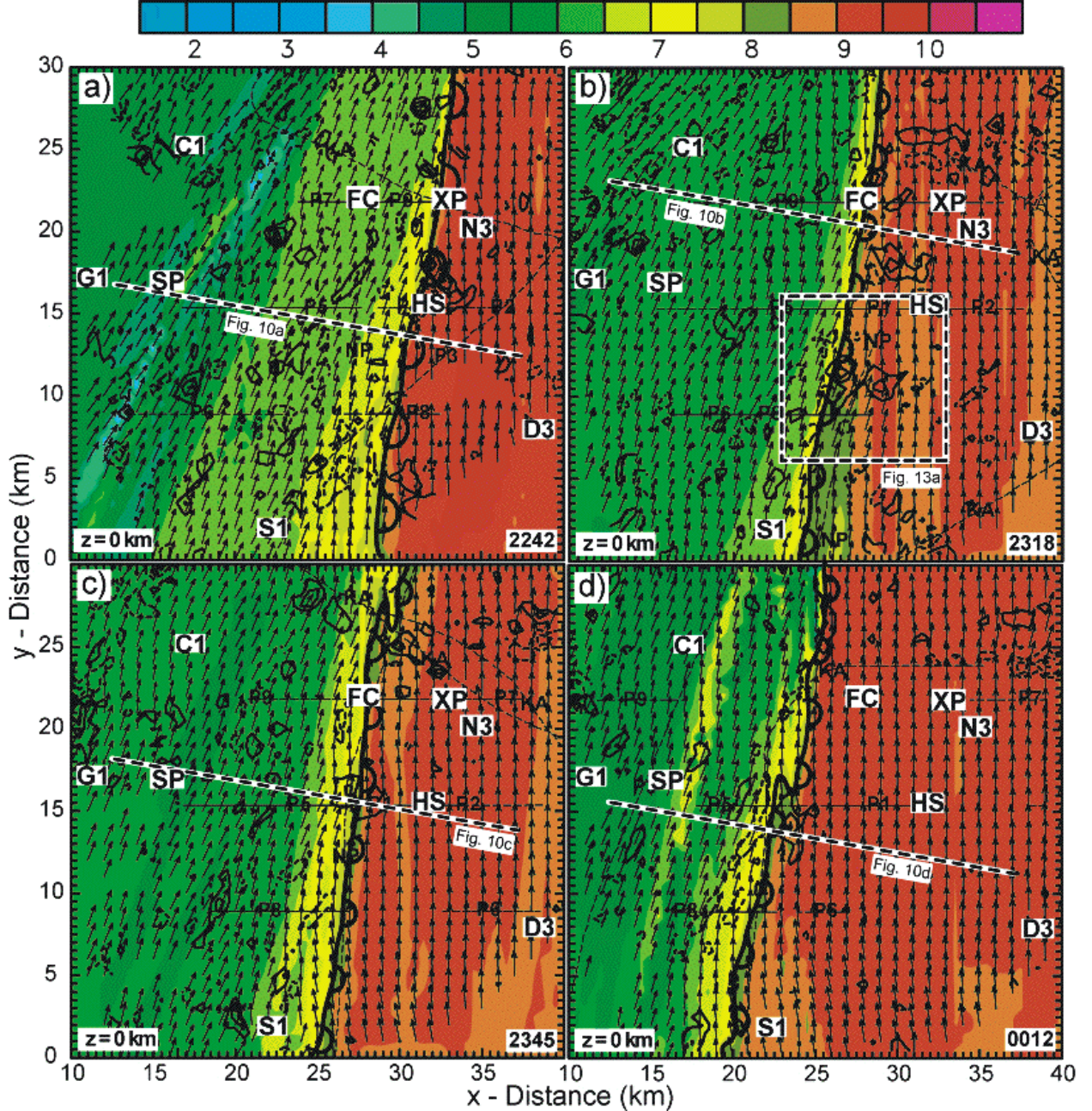


Figure 8. Surface Lagrangian water vapor mixing ratio (g kg^{-1}) analysis on 22 May 2002. Also plotted are horizontal wind vectors at every other grid point (with 1 km length equal to 15 m s^{-1}) and vertical vorticity (s^{-1}) every $3 \times 10^{-3} \text{ s}^{-1}$ with positive values (black solid lines) starting at $3 \times 10^{-3} \text{ s}^{-1}$ and negative values (black dotted line) starting at $-3 \times 10^{-3} \text{ s}^{-1}$. The thin black lines and curves indicate various mobile mesonet and aircraft traverses. The thick black dashed lines are the locations of cross-sections to be shown in figures 10-11 and the black dashed box is the location of Fig. 13.

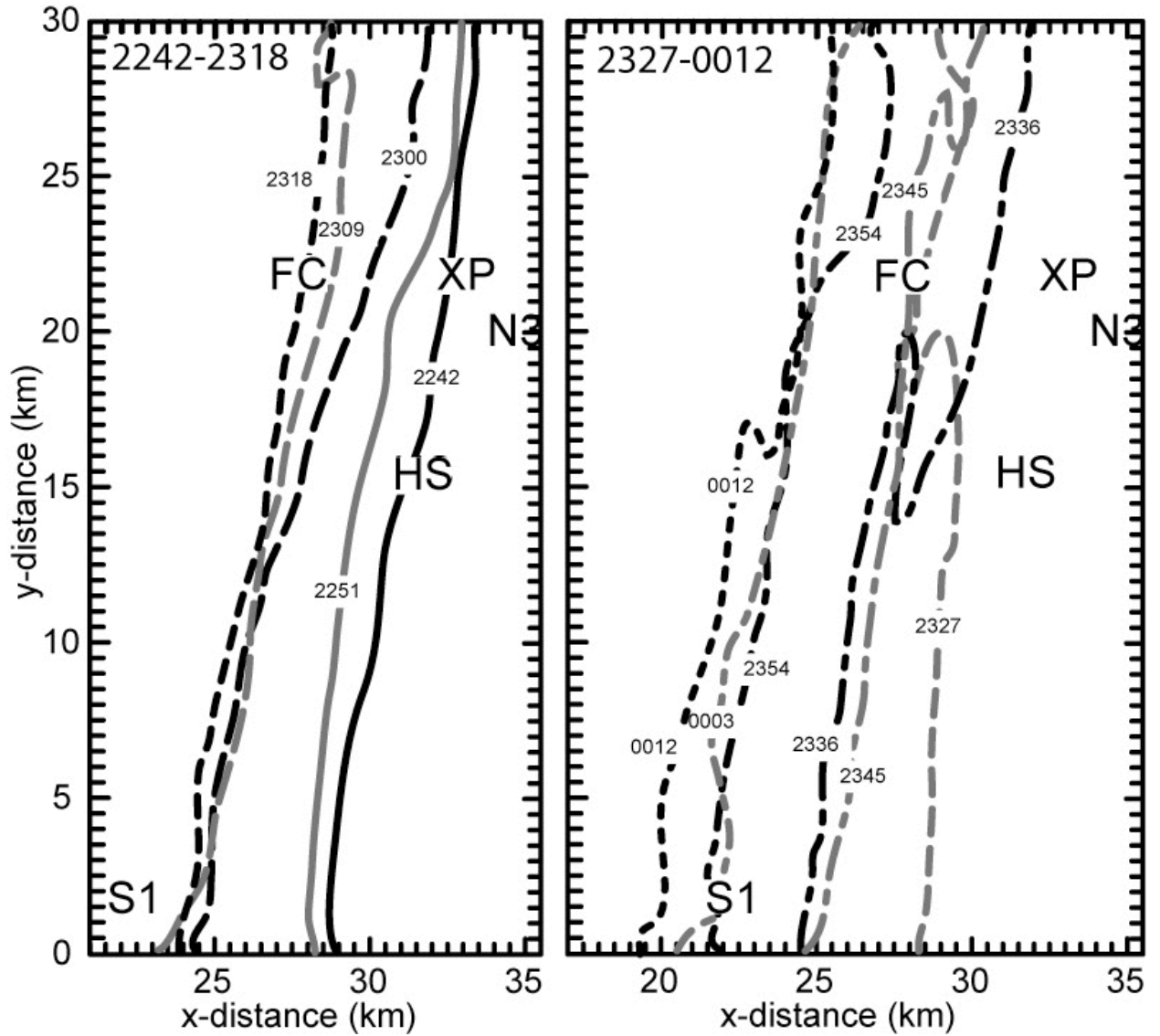


Figure 9. Isochrones of dryline position at 9 minute intervals from 2242-2318 UTC (left) and 2327-0012 UTC (right) obtained from the Lagrangian analyses on 22 May 2002.

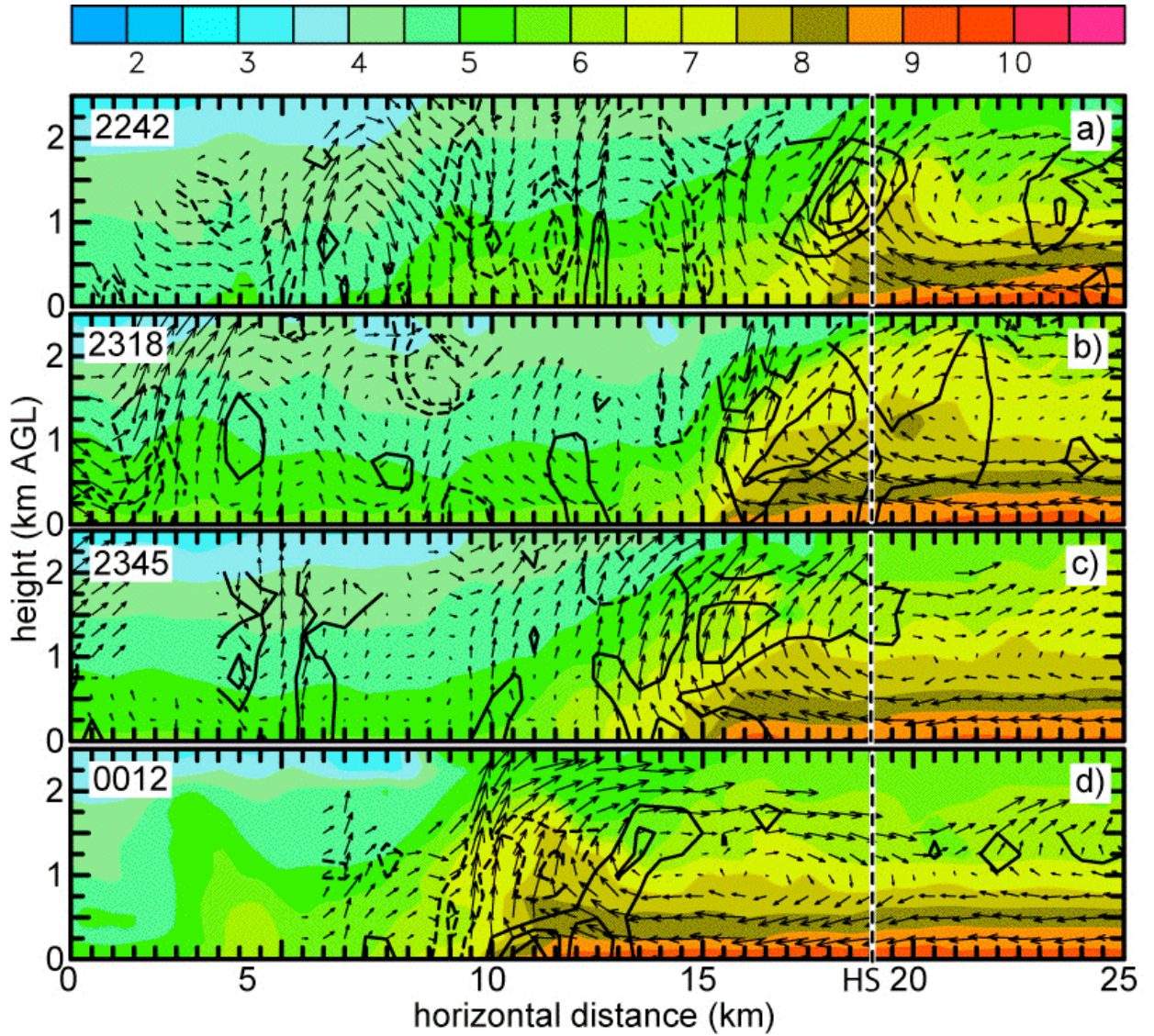


Figure 10. Vertical cross sections of water vapor mixing ratio (g kg^{-1}), wind vectors at every other grid point in the horizontal and every grid point in the vertical (with 1 km length equal to 15 m s^{-1}), and vertical vorticity every $3 \times 10^{-3} \text{ s}^{-1}$ with positive values (black solid lines) starting at $3 \times 10^{-3} \text{ s}^{-1}$ and negative values (black dashed line) starting at $-3 \times 10^{-3} \text{ s}^{-1}$. The black dashed vertical line shows the location of Homestead. Cross-section locations are shown in Figure 8.

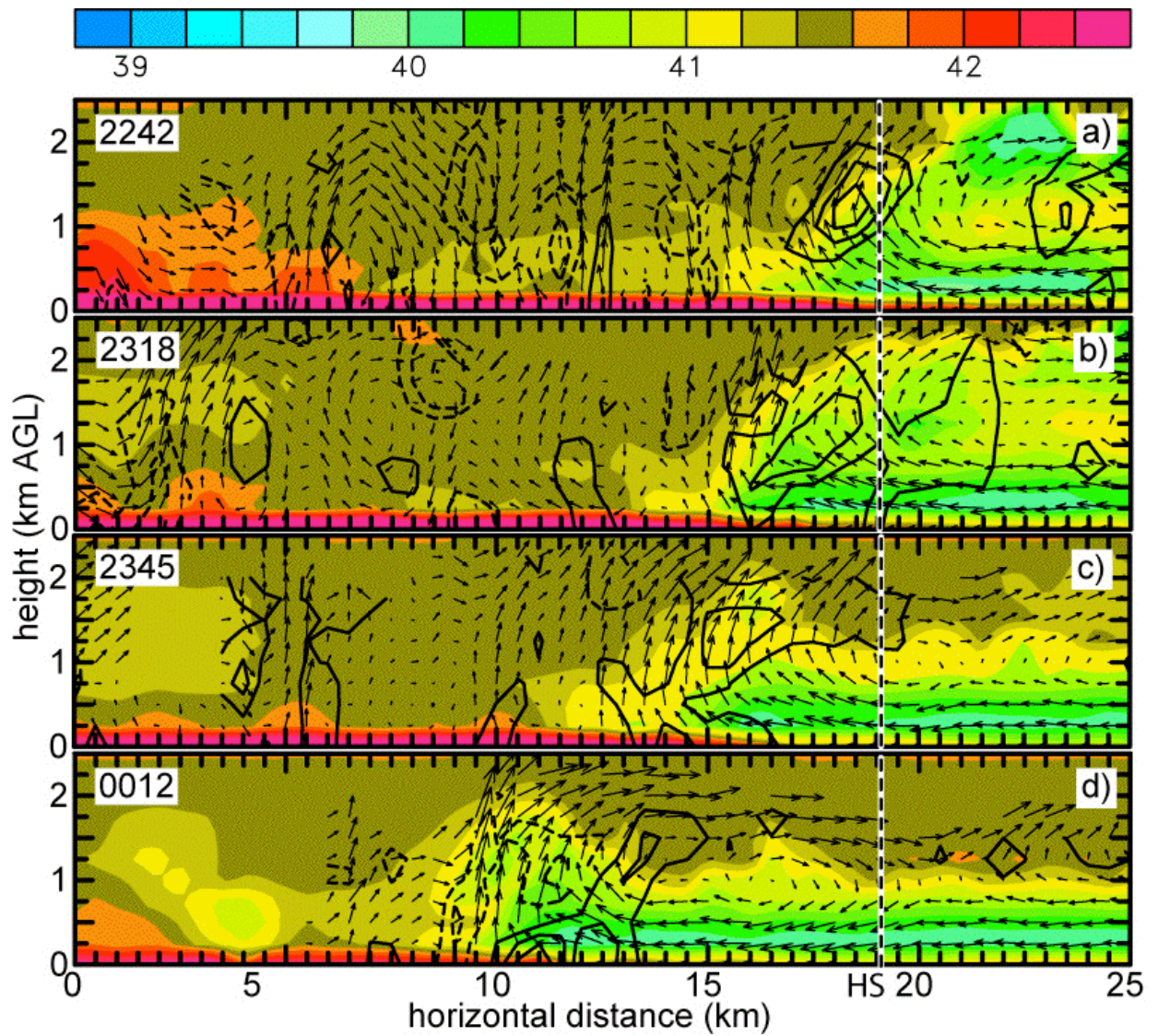


Figure 11. Same as in Fig. 10 except shaded areas are virtual potential temperature (K).

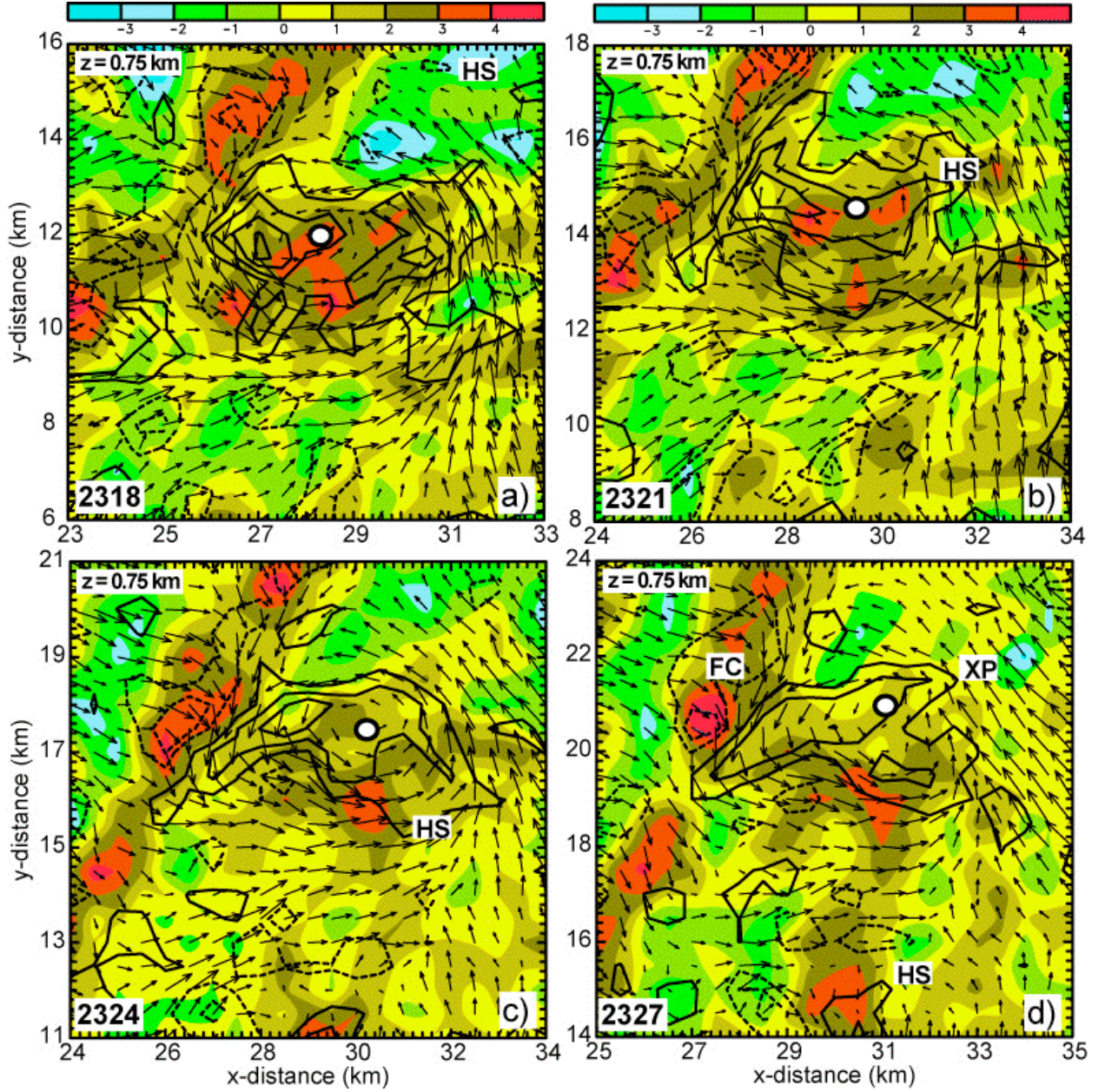


Figure 12. Same as in Fig. 5 except vectors plotted every grid point and negative (dotted line) and positive (solid line) vertical vorticity contoured every 2×10^{-3} starting at 2×10^{-3} . The white circle with black outline indicates the center of the vortex at each time. The locations of the grid at 2318 is shown in Fig. 3b.

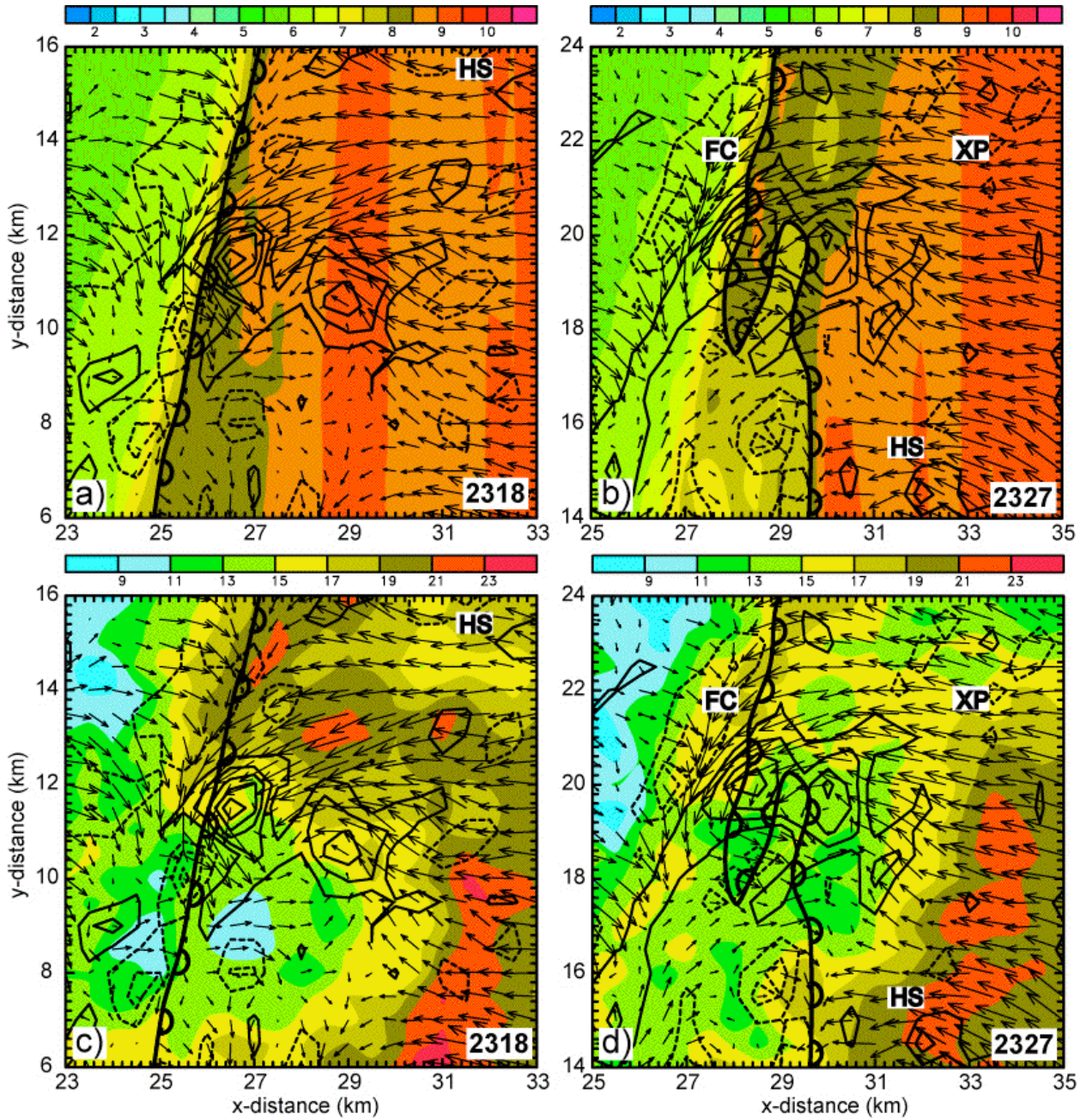


Figure 13. Horizontal vortex relative wind vectors (1 km=6 m s⁻¹), negative (dotted line) and positive (solid line) vertical vorticity contoured every 2 x 10⁻³ starting at 2 x 10⁻³. The shaded fields are water vapor mixing ratio (g kg⁻¹) every 0.5 g kg⁻¹ (top) and reflectivity (dBz) every 2 dBz (bottom) at 2318 and 2327 (left and right respectively). The locations of each grid are the same as in Fig. 12. Also shown are the dryline locations.